Buoyancy Arrest and Bottom Ekman Transport. Part I: Steady Flow

K. H. BRINK AND S. J. LENTZ

Department of Physical Oceanography, Woods Hole Oceanographic Institution, Woods Hole, Massachusetts

(Manuscript received 2 April 2009, in final form 14 September 2009)

ABSTRACT

It is well known that along-isobath flow above a sloping bottom gives rise to cross-isobath Ekman transport and therefore sets up horizontal density gradients if the ocean is stratified. These transports in turn eventually bring the along-isobath bottom velocity, hence bottom stress, to rest (''buoyancy arrest'') simply by means of the thermal wind shear. This problem is revisited here. A modified expression for Ekman transport is rationalized, and general expressions for buoyancy arrest time scales are presented. Theory and numerical calculations are used to define a new formula for boundary layer thickness for the case of downslope Ekman transport, where a thick, weakly stratified arrested boundary layer results. For upslope Ekman transport, where advection leads to enhanced stability, expressions are derived for both the weakly sloping (in the sense of slope Burger number $s = \alpha N/f$, where α is the bottom slope, N is the interior buoyancy frequency, and f is the Coriolis parameter) case where a capped boundary layer evolves and the larger s case where a nearly linearly stratified boundary layer joins smoothly to the interior density profile. Consistent estimates for the buoyancy arrest time scale are found for each case.

1. Introduction

In a stratified ocean, cross-isobath Ekman transport (associated with an along-isobath flow) causes vertical motions and therefore contributes to the development of a horizontal density gradient. In the initial stages of adjustment, turbulent mixing and dissipation are important; however, with time, a nonturbulent equilibrium can be established. Regardless of the upslope or downslope sense of the Ekman transport, the horizontal density gradient acts, through thermal wind balance, to bring the along-isobath velocity adiabatically toward rest at the bottom. These insights go back to at least Weatherly and Martin (1978, hereafter WM78) and have been further developed and refined by others (e.g., Thorpe 1987; MacCready and Rhines 1991; Trowbridge and Lentz 1991, hereafter TL91; MacCready and Rhines 1993; Garrett MacCready and Rhines 1993; Ramsden 1995, Middleton and Ramsden 1996, hereafter MR96). These authors all concentrated on an initial-value problem where a steady interior flow is suddenly started and then the boundary layer adjusts until there is no longer any along-isobath bottom stress.

Although the published results have presented increasingly refined estimates of boundary layer thickness and adjustment times, there is still room for improvement. For example, Lentz and Trowbridge (1991) point out that downslope Ekman transport leads to a bottom boundary layer that, although thickened because of gravitational instability, retains a finite stratification. Although this phenomenon was explored by MR96, they did not provide an expression for the boundary layer thickness that accounts accurately for this added stability. Further, previous authors have generally not dealt in much detail with the case of upwelling Ekman transport. In this case, there is competition between the stabilizing effects of upslope transport of dense water and the development of the turbulence that characterizes the evolving bottom boundary layer. Thus, one might expect that model results depend strongly on how a particular turbulence parameterization balances these competing effects.

We revisit the buoyancy arrest initial-value problem here to present two classes of results. First, we obtain general expressions for the Ekman transport and buoyancy shutdown time scales. Second, we derive new scales for boundary layer thickness (hence adjustment time) that account for finite boundary layer static stability in both the upwelling and downwelling cases. These results

Corresponding author address: K. H. Brink, Department of Physical Oceanography, Woods Hole Oceanographic Institution, Mail Stop 21, Woods Hole, MA 02543.
E-mail: kbrink@whoi.edu

DOI: 10.1175/2009JPO4266.1

are a necessary prelude to the development of models for time-dependent boundary layer flow above a sloping bottom (Brink and Lentz 2010, hereafter Part II).

2. Formulation

The ocean is assumed to have a constant initial vertical density gradient ρ_{Iz} everywhere and to lie above a sloping bottom at $z' = -h_0 + \alpha x'$. In a coordinate system where the z' axis is perfectly vertical, all fields are initially uniform in both x' (cross-isobath direction) and y' (along-isobath direction). The depth-independent interior flow v_I is purely along isobaths and is impulsively started at time $t = 0$. The equations of motion are rotated into a reference frame where z is perpendicular to the bottom, and the fields are broken into interior components (v_I and ρ_I) and boundary layer components (u_E, v_E, and ρ_E) that vanish far above the bottom. The equations governing the boundary layer variables, for small slope $\alpha \approx \sin\alpha$, then become (e.g., WM78)

$$u_{Et} - fv_E = -g\alpha\rho_E/\rho_0 + (Au_{Ez})_z, \tag{1a}$$

$$v_{Et} + fu_E = (Av_{Ez})_z, \quad \text{and} \tag{1b}$$

$$\rho_{Et} + u_E\alpha\rho_{Iz} = (K\rho_{Ez})_z, \tag{1c}$$

and the interior density component is governed by

$$\rho_{It} + u_I\alpha\rho_{Iz} = (K\rho_{Iz})_z. \tag{1d}$$

Subscripts with regard to an independent variable indicate partial differentiation; A and K are the eddy viscosity and eddy diffusivity, respectively; and u_E, v_E, and ρ_E are boundary layer rotated cross-isobath velocity, along-isobath velocity, and density, respectively. Here, f is the Coriolis parameter, α is the (constant, small) bottom slope, and g is the acceleration due to gravity. For all cases given here, $\alpha \geq 0$. Because diffusivity outside the bottom boundary layer is small, the diffusive term in (1d) is small there; therefore, the interior (well above the bottom boundary layer) buoyancy frequency squared is a constant, $N^2 = -g\rho_{Iz}/\rho_0$. The eddy coefficients are taken to depend on time and height. The beauty of this formulation is that a physically two-dimensional problem is reduced to a one-dimensional system.

Solutions to (1) are matched to a turbulent logarithmic layer at height $z = z_T$ above the physical bottom, so that

$$Au_{Ez} = c_D[(u_I + u_E)^2 + (v_I + v_E)^2]^{1/2}(u_I + u_E) \quad \text{and} \tag{2a}$$

$$Av_{Ez} = c_D[(u_I + u_E)^2 + (v_I + v_E)^2]^{1/2}(v_I + v_E), \tag{2b}$$

where

$$c_D = \left[\frac{\kappa}{\ln(z_T/z_0)}\right]^2 \tag{2c}$$

is the bottom drag coefficient. The bottom roughness is described by z_0, and $\kappa = 0.4$ is von Kármán's constant. Note that using this boundary condition assumes that the physical logarithmic layer is no thinner than z_T but that it can extend higher into the numerical grid. Other boundary conditions are that there is no density flux through the bottom and that $(Au_{Ez})_z = (Av_{Ez})_z = (K\rho_z)_z = 0$ far from the bottom (at the top of the grid, normally at least $z = 60$ m, when the problem is solved numerically). This upper density boundary condition is numerically convenient but does allow a small vertical flux because the background eddy diffusivity is nonzero (the alternative of no flux would disturb the linear density profile). The stress conditions are chosen for consistency and always result in no stress at the upper boundary.

Numerical solutions to the system (1) are obtained using implicit time stepping. In practice, (1c) and (1d) are added, so we solve for total density plus the boundary layer velocity components. The code is written such that the eddy coefficients can be found using a variety of closures: Mellor–Yamada 2.0 (as used by WM78), Mellor–Yamada 2.5, k–ε (both implemented as in Wijesekera et al. 2003), Pacanowski and Philander (1981), or constant coefficients. The Mellor–Yamada 2.5 scheme is used throughout the following unless otherwise noted. A sampling of runs was repeated with Mellor–Yamada 2.0 and with k–ε, and there were some quantitative differences (typically 20% or less in boundary layer thickness for Mellor–Yamada 2.0 versus either Mellor–Yamada 2.5 or k–ε, which tend to be very similar). Following WM78, a roughness height of $z_0 = 0.03$ cm is used in most examples given here. Several approaches were taken to the vertical grid scheme, including logarithmic spacing (as in WM78; Romanou and Weatherly 2001). The ultimate choice of scheme (after sensitivity studies) was a constant vertical grid spacing (20 cm) matched to a logarithmic layer at a height of $z_T = 50$ cm above the true bottom (combined with the choice $z_0 = 0.03$ cm, this yields $c_D = 0.0029$ for most of the model runs reported here). The advantage of the constant grid spacing is that it gives good resolution throughout the water column, so it does not "smear out" any density or velocity jumps across the top of the bottom boundary layer. Results here differ quantitatively from those of WM78 because of grid resolution, turbulence parameterization, and duration of model run.

All model runs reported here are at least 25 days in duration.

Two important nondimensional parameters arise from the system (1) (e.g., TL91). First, there is a Burger number,

$$s = \frac{\alpha N}{f}, \tag{3a}$$

which measures the importance of bottom slope (large s means that buoyancy transport effects are important in this problem). Second, there is a friction parameter,

$$d = c_D \frac{N}{f}. \tag{3b}$$

3. General considerations

a. Boundary layer transport

The bottom Ekman transport is substantially modified by effects of the bottom slope, even well before buoyancy arrest is reached. This result was stated by MR96, but a derivation is presented here to clarify the underlying assumptions and its generality. The system (1) is integrated from the bottom to some large height (where all boundary layer variables vanish) to yield

$$U_{\mathrm{Et}} - fV_E = -B_E\alpha - \tau^x/\rho_0, \tag{4a}$$

$$V_{\mathrm{Et}} + fU_E = -\frac{\tau^y}{\rho_0}, \quad \text{and} \tag{4b}$$

$$\left(\frac{\rho_0}{g}\right)B_{\mathrm{Et}} + \alpha\rho_{\mathrm{Iz}}U_E = K(0, t)\rho_{\mathrm{Iz}} \approx 0, \tag{4c}$$

where

$$U_E = \int u_E\, dz; \tag{4d}$$

$$V_E = \int v_E\, dz; \tag{4e}$$

$$B_E = \int \left(\frac{g\rho_E}{\rho_0}\right) dz; \tag{4f}$$

and (τ^x, τ^y) is the bottom stress, which is determined by potentially complex interactions between the interior and boundary layer flows. For most bottom boundary layer formulations, the turbulent mixing coefficients approach zero near the bottom, so we neglect the right-hand side of (4c).

Under steady conditions, (4b) reduces to the familiar bottom Ekman transport relation, but (4c) under steady conditions requires that $U_E = 0$, so that

$$fU_E = -\frac{\tau^y}{\rho_0} = 0, \tag{5}$$

as long as $\alpha\rho_{\mathrm{Iz}} \neq 0$. This is simply a statement that buoyancy arrest occurs in the bottom boundary layer (i.e., that the steady state has no Ekman transport).

We now consider the time-dependent version of (5) with an eye toward treating the buoyancy arrest problem. Straightforward manipulation of (4) yields

$$(f^2 + \alpha^2N^2)U_E + U_{\mathrm{Ett}} = \frac{(-\tau_t^x - f\tau^y)}{\rho_0} \quad \text{and} \tag{6a}$$

$$B_{\mathrm{Et}} = \alpha N^2 U_E. \tag{6b}$$

For buoyancy arrest problems, it is often reasonable to expect that the adjustment time scale T is long relative to the inertial time scale f^{-1}, so that, following TL91, the time derivatives in (6a), but not (6b), can safely be neglected. The result is a modified relation between bottom stress and boundary layer transport:

$$f^{*2}U_E = -\frac{f\tau^y}{\rho_0}, \tag{7a}$$

where

$$f^{*2} = (f^2 + \alpha^2N^2) = f^2(1 + s^2) \geq f^2. \tag{7b}$$

Thus, for slowly varying time-dependent stratified problems over a sloping bottom, the bottom Ekman transport is always weaker than would be expected for $s = 0$. For perfectly steady flow with stratified conditions over a sloping bottom, $U_E = 0$; however, the traditional nonzero expression for Ekman transport derived naively from (4b) should never be expected to hold for $s \neq 0$ until arrest occurs.

The sloping-bottom Ekman relation (7a) could be derived by neglecting the acceleration U_{Et} in (4a) but not V_{Et} in (4b). This slowly varying approximation filters out the natural oscillations at frequency near f^*. The discrepancy between (7a) and the traditional Ekman transport relation (5) is then clearly associated with the deceleration [in (4b)] of the along-isobath flow resulting from buoyancy adjustment. Specifically, inserting (7a) into (4b) yields

$$V_{\mathrm{Et}} - f^2\tau^y/(f^{*2}\rho_0) = -\frac{\tau^y}{\rho_0} \quad \text{and}$$

$$V_{\mathrm{Et}} = -\frac{\rho_0^{-1}\tau^y s^2}{(1 + s^2)}. \tag{8}$$

The natural oscillations in the system are simply near-inertial internal waves that propagate such that velocity normal to the bottom is zero. Examination of system (1) shows that the oscillations can have vertical phase shifts (as are sometimes evident in calculations) or frequencies differing from f^* only when the eddy viscosity is nonzero. Our calculations show that, in most cases where the

oscillations are present, the eddy viscosity peaks about once per cycle (in association with peaking shears) but is clearly not steady enough to be idealized as a constant.

b. Adjustment time scales

To estimate the arrest time scale, it is useful to hypothesize (motivated by MacCready and Rhines 1991) that, during the course of adjustment, the along-isobath bottom stress can be described by

$$\tau^y = \rho_0 u_0^{*2} \varphi, \tag{9a}$$

where

$$u_0^{*2} = b^2 c_D |v_I| v_I \tag{9b}$$

is the stress in the absence of any buoyancy arrest $b^2 = 0.4$ (Part II) and φ is an unknown dimensionless function of time that must approach zero for $t \to \infty$. Further, we assume that (9a) has a well-defined time integral from zero to ∞ (until buoyancy arrest).

$$\text{If} \quad \varphi = \varphi(t/T), \quad \text{then}$$
$$\int \varphi(t/T)\, dt = T \int \varphi(\xi)\, d\xi = T\Phi, \tag{10}$$

where the integration is from 0 to ∞ and Φ is an $O(1)$ constant. Then, integrating (6b) in time from zero to ∞ and substituting in (7a), (9a), and (10) yields the final state

$$B_{\mathrm{E}\infty} = -\alpha N^2 f^{*-2} f u_0^{*2} T\Phi. \tag{11}$$

Thus, if the final depth-integrated buoyancy change $B_{\mathrm{E}\infty}$ is known, it is straightforward to estimate the arrest time scale T. However, because the physical processes involved in upslope and downslope Ekman transport are rather different, we anticipate that there will be different φ functions (φ^U and φ^D, respectively) and time scales (T^U and T^D, respectively) in the two cases.

If the arrest function φ depends on more than one time scale, (10) and (11) are no longer valid; however, it can still be straightforward to estimate the adjustment time scale using the general logic leading to (11).

4. The downwelling case

In the case of a downwelling-favorable flow ($v_I > 0$), downslope Ekman transport gravitationally destabilizes the bottom boundary layer, and it becomes quite thick. A representative plot of the evolution of the density field in this case is shown in Fig. 1. After the onset of an interior flow, a capped bottom mixed layer forms and quickly deepens over the first half pseudoinertial period π/f^* (0.3 days). Not long after this initial phase, the upper part of the mixed layer starts to develop a continuous stratification, while the upper boundary of the layer continues to move upward. This continued growth, which is due to destabilizing downslope transport, is generally accompanied by substantial oscillations with frequency near f^* having amplitudes (for both u and v) of typically 2–10 cm s^{-1}. During this extended growth phase, there is generally not a density cap at the top of the bottom boundary layer, although some long runs do develop a weak density cap, evidently because of entrainment related to oscillation-induced shear at the top of the boundary layer. After buoyancy adjustment is completed (see Fig. 2, heavy line, for a computed example), the density field, averaged over an oscillation period, is continuously stratified in the boundary layer, with density and velocity structures like those sketched in Fig. 3.

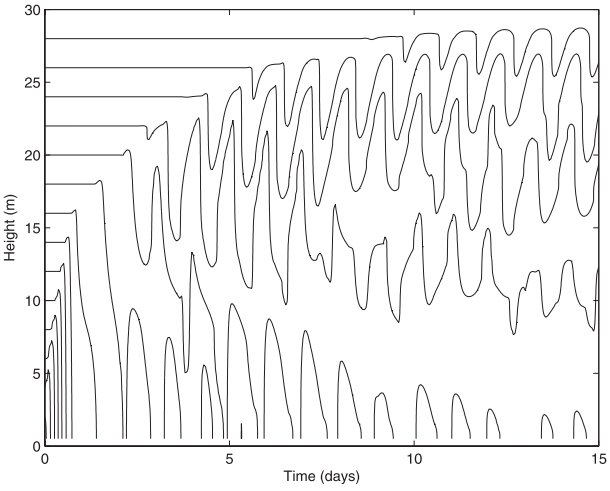

FIG. 1. Time–height contours of total density (contour interval = 0.000 02 gm cm^{-3}) for downwelling model run 89c ($s = 0.98$).

TL91 show that, if the steady, arrested boundary layer is perfectly well mixed, its thickness is

$$h^{\mathrm{TL}} = \frac{v_I}{(N s)}. \tag{12}$$

However, TL91 and Lentz and Trowbridge (1991) note that observations frequently show that the bottom boundary layer associated with downwelling-favorable alongshore flow is weakly but stably stratified. The occurrence of stratification in the boundary layer might be expected because, as Tandon and Garrett (1994) point out, a geostrophically adjusted boundary layer, in the presence of lateral density gradients, is expected to have a Richardson number >0.25. MR96 considered this stability effect, but they assumed small s and consequently simply recovered h^{TL} for the layer thickness.

The boundary layer stratification is modeled here by hypothesizing that the time-averaged (over a natural

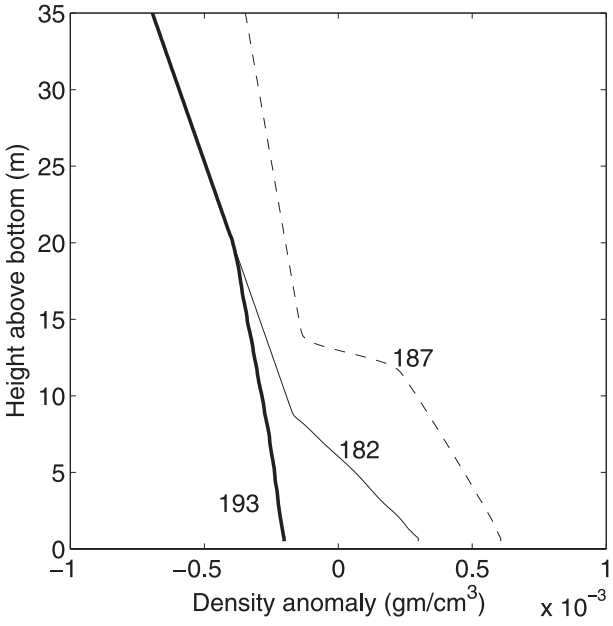

FIG. 2. Final (arrested) state density, averaged over a natural oscillation period, for downwelling run 193 (heavy line; $s = 1.38$) and for upwelling runs 182 (solid curve; $s = 1.38$; a smooth profile) and 187 ($s = 0.33$; a capped profile).

oscillation period) gradient Richardson number $\mathrm{Ri} = N^2/|v_{\mathrm{Ez}}|^2$ is constant within the boundary layer. Within the layer, shear and stratification are also taken to be constant. Outside the boundary layer, the ambient density (which is also the initial density) is given by

$$\rho_I = \rho_0 + \rho_{\mathrm{Iz}} z, \tag{13}$$

so the total density gradient within the bottom boundary layer (see Fig. 3) is $\rho_{\mathrm{Bz}} + \rho_{\mathrm{Iz}}$. The total density difference across the boundary layer $\delta\rho$ is

$$-\frac{\delta\rho}{h} = \rho_{\mathrm{Ez}} + \rho_{\mathrm{Iz}}, \tag{14}$$

where h is the boundary layer thickness. The boundary layer component of density is then (with the constant of integration chosen so that $\rho_E = 0$ at the top of the boundary layer)

$$\rho_E = (h - z)\rho_{\mathrm{Iz}} + \delta\rho\left[\frac{(h - z)}{h}\right]. \tag{15}$$

The boundary layer component of along-isobath flow, in the final state, is geostrophically balanced, so that (1a), with no remaining mixing or time dependence, is

$$-fv_E = -\frac{g\alpha\rho_E}{\rho_0}. \tag{16}$$

Thus,

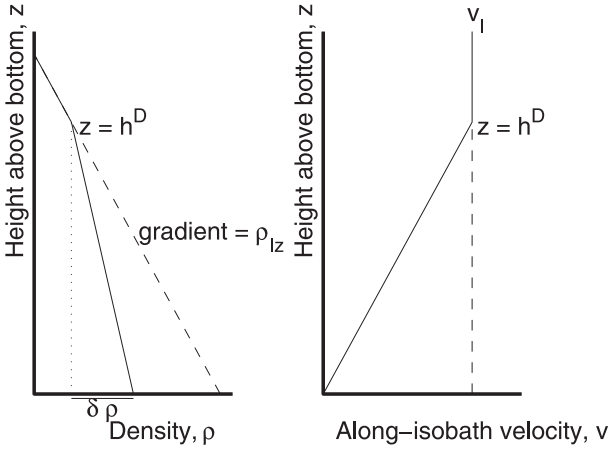

FIG. 3. Sketch of the geometry for a fully adjusted downwelling ($v_I > 0$) bottom boundary layer: (left) total density and (right) total velocity.

$$-fv_{\mathrm{Ez}} = \frac{\alpha g(\rho_{\mathrm{Iz}} + \delta\rho/h)}{\rho_0} \tag{17}$$

or, because the shear is constant at $v_{\mathrm{Ez}} = v_I/h$,

$$\frac{fv_I}{h} = \alpha N^2 - \frac{g\alpha\delta\rho}{(h\rho_0)}; \tag{18}$$

therefore,

$$h = \frac{(fv_I + g\alpha\delta\rho/\rho_0)}{(\alpha N^2)}. \tag{19}$$

Insisting that the gradient Richardson number

$$\mathrm{Ri} = -\frac{g(\rho_{\mathrm{Ez}} + \rho_{\mathrm{Iz}})}{(\rho_0 v_{\mathrm{Ez}}^2)} \tag{20}$$

(which neglects u_{Ez} as being very small in the steady state) is constant at a critical value Ri^D, using (14), and estimating $v_{\mathrm{Ez}} = v_I/h$ then closes the problem by requiring that

$$\delta\rho = \frac{\rho_0 \mathrm{Ri}^D v_I^2}{(gh)}. \tag{21}$$

Using (21) in (19) and then solving for h yields (using the positive root in the quadratic)

$$\begin{aligned} h^D &= [v_I/(2Ns)]\,[1 + (1 + 4\mathrm{Ri}^D s^2)^{1/2}] \\ &= [v_I/(Ns)]\Gamma(s), \end{aligned} \tag{22}$$

where

$$\Gamma(s) = \frac{\left[1 + (1 + 4\mathrm{Ri}^D s^2)^{1/2}\right]}{2} \geq 1. \tag{23}$$

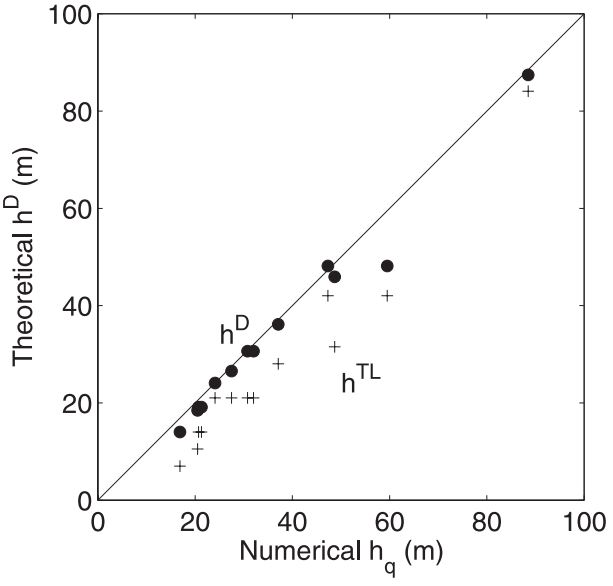

FIG. 4. Comparison of theoretical downwelling boundary layer thickness h^D (theoretical) vs results from numerical model runs (numerical) using Mellor–Yamada 2.5 turbulence closure. Crosses represent the model of TL91 result (12), and solid circles represent the present model result (22). The numerical results presented here are from model runs of 25–200-days duration, depending on the time needed to adjust to a steady layer thickness.

Thus, the TL91 result (which is the $\mathrm{Ri}^D = 0$ limit of 22) is always an underestimate relative to the present formulation. The superscript D is introduced as a reminder that its numerical value is specific to the downwelling case, averaged over a free oscillation period.

The predicted boundary layer thickness is compared to h_q, the height above the bottom where turbulent kinetic energy vanishes (WM78), from numerical model calculations (Fig. 4; Table 1). Results are only used here when the model has been run long enough to reach a steady boundary layer thickness. Because there is little or no density jump at the top of the adjusted bottom boundary layer (Figs. 1–3), h^D is most readily associated with h_q rather than, for example, the height where density stratification is at a maximum h_ρ. A least squares fit of (22) to the numerically calculated thickness h_q yields $\mathrm{Ri}^D = 0.7$. The present results are a substantial improvement over the earlier TL91 formulation (crosses in Fig. 4). The current model yields an rms difference (h^D versus numerical results) of 3.5 m, whereas the TL91 rms difference is 10.0 m for 13 runs. The one outlier on Fig. 4 is a case where a density cap forms at the top of the layer at large times. This cap is evidently associated with shear because of the continuing (and even growing) natural oscillations. The somewhat large gradient Richardson number (0.7) applies to density and velocity fields averaged over an oscillation period, whereas the instantaneous values within the boundary layer (not shown) span a much wider range of values.

The optimal Richardson number depends upon the turbulent mixing scheme. For example, experiments using the Philander and Pacanowski scheme (where the parameter dependence is relatively clear-cut) yield an Ri^D range of 0.8–2.1 over a reasonable range of maximum eddy viscosities and cutoff Richardson numbers (larger Ri^D for larger maximum viscosity, and for larger cut off Richardson number). Repeated runs with Mellor–Yamada 2.0 and 2.5 and with k–ε models suggest that a reasonable uncertainty for Ri^D is about 15% among the more realistic closure models.

Given the downwelling boundary layer structure conjectured earlier, it is straightforward to estimate the integrated boundary layer density in the final, arrested state. Specifically (Fig. 3), from (15), using (17) to replace $\delta\rho/h$, and the condition that $\nu = 0$ at the bottom (so that $v_{\mathrm{Ez}} = v_I/h$),

$$\rho_{E\infty} = -[\rho_0 f v_I/(g\alpha)](h^D - z)/h^D, \qquad (24)$$

TABLE 1. Downwelling Ekman transport model runs (only equilibrated runs are listed).

Run No.	$N^2 \times 10^4$ (s^{-2})	$f \times 10^4$ (s^{-1})	v_I (cm s^{-1})	a	s	d	h_q (m)	h^D (m)
81	0.9515	1.00	20.0	0.0050	0.49	0.28	47.3	48.2
82	0.9515	1.00	20.0	0.0025	0.24	0.28	88.5	87.4
84	0.9515	1.00	20.0	0.0100	0.98	0.28	32.0	30.6
86	0.9515	1.00	10.0	0.0050	0.49	0.28	24.1	24.1
89b	1.9029	1.00	20.0	0.0050	0.69	0.40	27.5	26.6
89c	0.9515	0.50	20.0	0.0050	0.98	0.57	30.8	30.6
190	2.8544	1.00	20.0	0.0050	0.84	0.49	21.3	21.1
191	2.8544	1.00	20.0	0.0100	1.69	0.49	16.9	16.9
192	0.9515	1.00	30.0	0.0100	0.98	0.28	48.7	43.3
193	1.9029	1.00	20.0	0.0100	1.38	0.40	20.5	20.5
194	0.9515	1.00	20.0	0.0075	0.73	0.28	37.1	36.7
195	2.8544	0.50	20.0	0.0025	0.84	0.98	20.7	20.3
196	0.9151	1.00	20.0	0.0050	0.49	0.28	59.5	59.1

so that

$$B_{E\infty} = -0.5(fv_I/\alpha)h^D \tag{25a}$$

$$= -0.5(v_I^2/s^2)\Gamma(s). \tag{25b}$$

For downwelling, the numerical model results are consistent with the form $\varphi = \varphi(t/T)$, so (10) and (11) are valid. Substitution of (25) into (11) then yields the downwelling arrest time scale

$$|\Phi^D T^D| = \Gamma(s)(1+s^2)(2fb^2ds^3)^{-1}, \tag{26}$$

where Φ^D is an unknown and $O(1)$ is constant. This time-scale estimate can be compared with that of MR96 (in our notation):

$$T^{\mathrm{DMR}} = \frac{(1+s^2)(1-\mathrm{Ri}^{\mathrm{MR}}s^2)}{(fs^3d)}. \tag{27}$$

Their Richardson number is $\mathrm{Ri}^{\mathrm{MR}} \approx 0.15$. The primary difference between the two formulations is replacement of $\Gamma(s)$ in (26) with $(1 - \mathrm{Ri}^{\mathrm{MR}}s^2)$, a rather curious contrast that is evidently related to their small s expansion and perhaps to some notational issues.

It is straightforward to test the conjectured temporal scaling (26) for the downwelling case by using outputs from the downwelling numerical model runs summarized in Table 1, plus two unequilibrated runs. Specifically, for each model run, a time series of along-isobath bottom stress τ^y (each plotted value being the average over an oscillation period $2\pi/f^*$) is obtained, and its amplitude is then normalized by the stress that would exist if there were no bottom slope, $b^2c_D|v_I|v_I$. Then, the time scale for each run is normalized by $\Phi^D T^D$ from (26). The binned mean curve is then integrated to obtain $\Phi^D = 0.81$, and the model time is then renormalized by only T^D. Both the unscaled and normalized time series are shown in Fig. 5 (positive values). The collapse of the 15 time series onto a single curve (bottom panel) is quite striking, with a nondimensional rms scatter about the binned mean curve of about 0.008 for nondimensional time <5.

5. The upwelling case

a. Overview

When $v_I < 0$, the bottom Ekman transport carries water upslope and the bottom boundary layer becomes increasingly stable. Thus, the final layer is thinner than in the case with a flat bottom, where turbulence is not so strongly inhibited. MR96 observed this tendency toward shallower bottom mixed layers in their model runs and found empirically that their results were fit well by the functional form (in our notation)

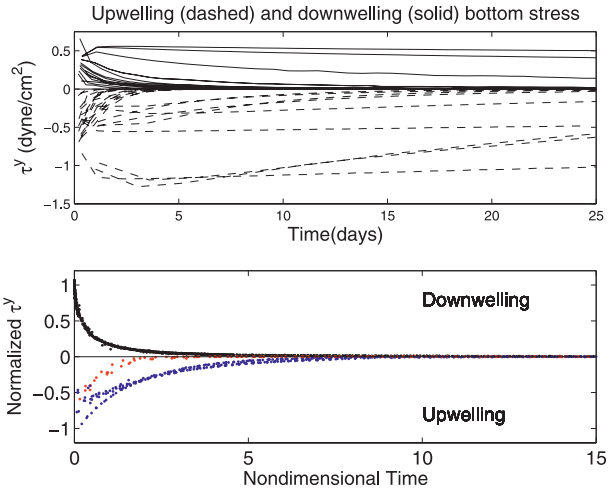

FIG. 5. (top) Bottom stress for a variety of model runs as a function of dimensional time and (bottom) nondimensionalized stress (by $\rho_0 c_D b^2 v_I^2$) vs nondimensional time for initial-value problems with steady flow imposed. Solid lines (positive stresses) in (top) result from the downwelling problem ($v_I > 0$), and dashed lines result from upwelling ($v_I < 0$). (bottom) Black dots are values from downwelling runs, red dots are from upwelling smooth runs, and blue dots are from upwelling capped runs. All time series are smoothed by averaging over successive natural oscillation periods. Time is nondimensionalized by T^{US} [in (37)] or T^{UC} [in (45)] for the upwelling cases and by T^D [in (26)] for the downwelling case. Upwelling runs with $s < 0.1$ are not included, because they appear to obey a different temporal scaling.

$$h^{\mathrm{MR}} = h_0^F(1+s)^{-1}, \tag{28a}$$

where (e.g., Thompson 1973)

$$h_0^F = (2R_b)^{1/4}u_0^*(fN)^{-1/2} = \frac{bc\,|v_I|d^{1/2}}{N} \tag{28b}$$

is the turbulent bottom boundary layer thickness over a flat bottom (superscript F is to point out that this is for a flat bottom and subscript 0 accentuates that this is for zero frequency), R_b is a bulk Richardson number, and $c = (2R_b)^{1/4}$. MR96 did not provide a derivation for (28a). Given their form for the boundary layer thickness, it is straightforward to approximate $B_{E\infty}$ by the upwelling equivalent of (25a) and use (28a) in (11) to derive their buoyancy adjustment time for upwelling

$$|\Phi^{\mathrm{MR}} T^{\mathrm{MR}}| = (1+s^2)[(1+s)s^2fd^{1/2}]^{-1}. \tag{29}$$

Our numerical model runs for upwelling typically show two different end states when results are averaged over a natural oscillation period (Fig. 2). For large s (large nondimensional bottom slope), run 182 (light solid line in Fig. 2) is typical: density varies linearly with height

within the bottom boundary layer and this profile connects directly to the linearly stratified interior region. We call this type of adjusted density profile "smooth." In other cases, where s is smaller (e.g., run 187: the dashed line in Fig. 2), the final density profile always consists of linearly stratified regions within and outside of the bottom boundary layer; however, they are separated by a sharp density jump across the top of the layer. We call this type of profile "capped," and it appears to include all of the MR96 upwelling runs (e.g., their Figs. 6, 8). Over a flat bottom, there is typically a sharply defined bottom mixed layer (e.g., Thompson 1973; WM78), so a cap is expected, although a density gradient below the cap would not be found over a flat bottom.

The two cases have somewhat different time evolutions. In the smooth case (Fig. 6a), the buoyancy adjustment occurs quickly, as might be expected from (29) for large s: stratification is reestablished at all depths by around day 1. Initially, a bottom mixed layer is formed, as would be expected in a turbulent bottom boundary layer before the stabilizing effects of lateral density advection are felt. The transient bottom mixed layer is capped by a sharp density gradient. However, around day 0.5, the boundary layer (defined, in this figure, as the height to which otherwise horizontal isopycnals are disturbed) suddenly thickens by about 1 m beyond the initial mixed layer depth and the upper part of the boundary layer becomes continuously stratified. From this time, the top of the bottom boundary layer is no longer characterized by a density jump. With time, the stratified region spreads downward from the top of the bottom boundary layer toward the bottom. The remaining mixed layer is where the remaining Ekman transport occurs, and it becomes denser and thinner with time, whereas its density cap increasingly weakens. Its instantaneous thickness is evidently governed by a bulk Richardson number criterion. Throughout the process, oscillations at a frequency near f^* are prominent in the stabilized part of the boundary layer. All of the smooth model runs follow the same pattern of a jump in boundary layer thickness, stabilization from the top down, an internal density jump that eventually vanishes, and prominent oscillations.

In the capped case (Fig. 6b), adjustment time scales are typically much longer, as would be expected from (29) with smaller values of s. In this case, a bottom mixed layer forms with a distinct density cap that becomes somewhat less sharp with time but persists at the depth established early on (by day 5 in this example). At some time (day 6 here), the outer part of the boundary layer begins to stabilize, and the bottom mixed layer (which does not itself have a sharp density cap) becomes increasingly thin with time. The instantaneous thickness of the mixed layer within the bottom boundary layer scales

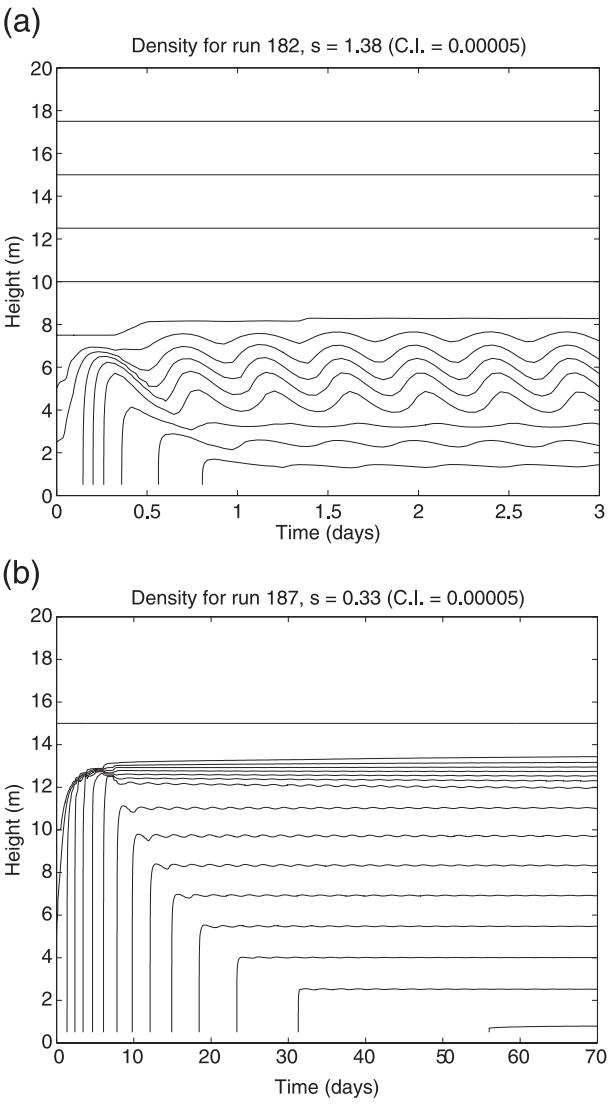

FIG. 6. Time–height contours of total density (contour interval = 0.000 05 gm cm^{-3}) for (a) run 182 ($s = 1.38$), a smooth upwelling ($\nu_I < 0$) case, and (b) run 187 ($s = 0.33$), a capped upwelling ($\nu_I < 0$) case. Note the difference in time scale between (a) and (b).

roughly as instantaneous u^*/f^*: that is, like the thickness of a turbulent Ekman layer in an unstratified fluid (e.g., Wimbush and Munk 1970). Thus, as the bottom stress weakens, the advecting Ekman layer thins as well, leaving behind continuously stratified waters. Unlike the smooth case, there is no transitory density jump within the bottom boundary layer, only the enduring jump at the top of the layer. Invariably, in the capped cases, the bottom mixed layer reaches a steady thickness before internal stabilization begins. The final, adjusted state below the density cap is typified by highly stable, nearly linear, stratification: gradient Richardson numbers here are well into the stable range.

b. The smooth upwelling bottom boundary layer

Following the example of the downwelling bottom boundary layer (section 4) and based on the numerical model results, we conjecture that the fully arrested smooth upwelling bottom boundary layer (averaged over an oscillation period) has a constant gradient Richardson number, it is geostrophically balanced, and that density and along-isobath velocity vary linearly with height in the adjusted layer. Thus,

$$v_{\mathrm{Ez}} = \frac{v_I}{h} \quad \text{and} \tag{30}$$

$$\rho_z = \rho_{\mathrm{Iz}} + \rho_{\mathrm{Ez}}, \tag{31}$$

where

$$\rho_{\mathrm{Ez}} = \frac{[0 - f v_I \rho_0/(g\alpha)]}{h}. \tag{32}$$

The bottom density in (32) follows from geostrophy in the bottom boundary layer [(1a) with no time dependence or dissipation] and by the requirement that $v_E = -v_I$ at the bottom. Forms (30)–(32) can be used to express a gradient Richardson number

$$\mathrm{Ri} = -\frac{g\rho_z}{(\rho_0 v_z^2)} \tag{33}$$

to obtain

$$h^{\mathrm{US}} = \left[-\frac{v_I}{(sN)}\right]\Lambda(s), \tag{34}$$

where

$$\Lambda = \frac{\left[-1 + (1 + 4\mathrm{Ri}^U s^2)^{1/2}\right]}{2}. \tag{35}$$

Numerical experiment shows that $\mathrm{Ri}^U = 0.4$ yields satisfactory results (again, the U superscript is a reminder that the specific numerical value applies to the upwelling case, averaged over an oscillation period). Spot checks using Mellor–Yamada 2.0 closure or with k–ε closure yield the same Richardson number. Note the striking resemblance of this form (except for the replacement of Γ by the complementary Λ) to that describing the destabilized downwelling case (22). TL91, in their Eq. (19), anticipate a similar sort of symmetry, although based on the differing assumption of a bottom well-mixed layer.

Finally, it is straightforward to calculate

$$B_{\mathrm{E}\infty} = 0.5 h^{\mathrm{US}} \frac{g\rho_E(0, \infty)}{\rho_0} = 0.5 h^{\mathrm{US}} \frac{f v_I}{\alpha} \tag{36}$$

so that, assuming that $\varphi = \varphi(t/T)$ and using (11),

$$|\Phi^{\mathrm{US}} T^{\mathrm{US}}| = \frac{0.5(1 + s^2)\Lambda}{(b^2 s^3 df)} \tag{37}$$

for the smooth upwelling case. Calculations show that $\Phi^{\mathrm{US}} = -0.42$. This time scale differs radically from that of MR96 (29), which is not surprising, given that their results seem to hold only for the capped case.

c. The capped upwelling bottom boundary layer

In the capped upwelling case, the boundary layer thickness, as defined by h_ρ, the height of the maximum density gradient, is usually established early on and always before the interior of the boundary layer begins to stabilize. Model runs with $s < 0.1$ show continual mixed layer deepening over many days until thickness (cap height) reaches a height approaching that which would be obtained over a flat bottom after a long time (see appendix). Otherwise, for $s > 0.1$, the stable mixed layer thickness is usually reached quickly, in no more than a few inertial periods. Thus, the boundary layer thickness is the result of a mixed layer process, where the thickness is expected to be set by a critical bulk Richardson number. We thus need to determine the density and velocity jumps across the top of the boundary layer for the time at which the thickness is established.

The boundary layer density is governed by boundary layer entrainment and by upslope advection of dense water by the bottom Ekman transport (6b). Thus, at any given time, the density jump across the top of the bottom boundary layer is

$$\delta\rho = 0.5 h \rho_{\mathrm{Iz}} + \left(\frac{\rho_0}{g}\right)\frac{B_E}{h} = 0.5 h \rho_{\mathrm{Iz}} - \alpha \rho_{\mathrm{Iz}} \int U_E \, dt/h. \tag{38}$$

Likewise, the shear across the top of the mixed layer is dominated by that associated with the Ekman transport, so

$$\delta v \approx \frac{U_E}{h}. \tag{39}$$

The time at which these relations are to be applied has not yet been determined, but we conjecture that the appropriate time is half of a natural oscillation period $t_0 = \pi/f^*$, the approximate time of maximum U_B, hence shear across the mixed layer cap. Further, at $t_0 = \pi/f^*$, we assume that the Ekman transport has not yet undergone substantial buoyancy arrest. With these assumptions, the governing density (38) and velocity (39) jumps across the top of the mixed layer become

$$\delta\rho \approx 0.5h\rho_{\mathrm{Iz}} - \{\alpha\rho_{\mathrm{Iz}}u_0^{*2}/[fh(1+s^2)]\}(0.5\,\pi/f^*) \quad \text{and} \tag{40}$$

$$\delta v \approx \frac{u_0^{*2}}{[fh(1+s^2)]}. \tag{41}$$

The boundary layer thickness is then determined by the bulk Richardson number criterion

$$R_b = \frac{gh\delta\rho}{(\rho_0\delta v^2)} \tag{42}$$

applied at time t_0. The result [using (40) and (41) in (42)] is a single equation for boundary layer thickness

$$0 = h^4 + h^2\alpha\pi\,u_0^{*2}/[f^2(1+s^2)^{1.5}] - h_0^{F4}(1+s^2)^{-2}, \tag{43a}$$

where, from (28b),

$$h_0^F = \frac{(2R_b)^{1/4}u_0^*}{\sqrt{(fN)}} \tag{43b}$$

is the boundary layer thickness that would occur if the bottom were flat.

It is straightforward to solve (43a) to obtain the capped boundary layer thickness,

$$h^{\mathrm{UC}} = \left[\frac{h_0^F}{(1+s^2)^{1/2}}\right][(1+\beta^2)^{1/2} - \beta]^{1/2}, \tag{44a}$$

where

$$\beta = \frac{s\pi}{[2(2R_b)^{1/2}(1+s^2)^{1/2}]}. \tag{44b}$$

The buoyancy adjustment time is now estimated using (36) to approximate $B_{\mathrm{B}\infty}$ and (11),

$$|\Phi^{\mathrm{UC}}T^{\mathrm{UC}}| = (1+s^2)^{1/2}(fs^2d^{1/2})^{-1}[(1+\beta^2)^{1/2} - \beta]^{1/2} \times [0.5(2R_b)^{1/4}/b]. \tag{45}$$

The approach used in section 4 yields $\Phi^{\mathrm{UC}} = -1.52$.

Expression (44a) is not valid for those runs where mixed layer thickness grows past h_0^F or h^{UC}. In the case of a perfectly flat bottom (see appendix), cross-isobath advection does not stabilize the bottom boundary layer at all and shear across the top of the mixed layer is not the only source of turbulence. The result is a bottom boundary layer that thickens over a much longer time scale than π/f^*. These continually thickening cases occur when the stabilizing influence of density advection in the bottom boundary layer is negligible at the "control time" $t_0 = \pi/f^*$, so a minimal (and probably insufficient) criterion for boundary layer depth exceeding h^{UC} (from 38) is

$$-0.5h\rho_{\mathrm{Iz}} \gg \left(\frac{\rho_0}{g}\right)\frac{B_E}{h} \quad \text{at} \quad t_0 = \frac{\pi}{f^*}, \tag{46a}$$

which reduces to

$$\left(\frac{h^{\mathrm{UC}}}{h_0^F}\right)^2 \gg s\beta/2, \tag{46b}$$

or, for small s^2,

$$1 \gg s^2\left[\frac{0.25\pi}{(2R_b)^{1/2}}\right]. \tag{46c}$$

Note that expressions (46b) and (46c) depend only on s and not on the nondimensional bottom drag d. In practical terms, we find that mixed layer thickness continues to grow beyond h^{UC} when, roughly, $s < 0.1$.

It is necessary to define when h^{US} or h^{UC} is the correct choice of upwelling boundary layer thickness. Our numerical results show that the correct expression for the final upwelling boundary layer thickness is

$$\begin{aligned} &h > h^{\mathrm{UC}} \quad \text{for} \quad s < 0.1, \\ &h = h^{\mathrm{US}} \quad \text{if} \quad h^{\mathrm{US}} > h^{\mathrm{UC}}, \\ &h = h^{\mathrm{UC}} \quad \text{if} \quad h^{\mathrm{UC}} > h^{\mathrm{US}}. \end{aligned} \tag{47}$$

We used 23 upwelling numerical model runs (both smooth and capped) with $s > 0.1$ to estimate the Richardson numbers (Table 2). The pair $R_b = 2$, $\mathrm{Ri}^U = 0.4$ yields an overall rms error for h of 1.61 m with a correlation of 0.99 (Fig. 7).

The separation between the capped and smooth cases expressed by (47) can be expressed quantitatively by using (34) and (44): that is, the boundary layer is capped if

$$h^{\mathrm{UC}} > h^{\mathrm{US}} \quad \text{or} \quad d > \frac{\Lambda^2(1+s^2)}{\{s^2c^2b^2[(1+\beta^2)^{1/2} - \beta]\}}, \tag{48}$$

where $c = (2R_b)^{1/4}$. The resulting regime diagram for upwelling boundary layer structure is shown in Fig. 8. Physically, the smooth boundary layer structure occurs when the capped boundary layer cannot bring the bottom flow geostrophically to rest without incurring a gradient Richardson number (for the time-averaged density and velocity) below the critical value of 0.4. This minimum value can be maintained (i.e., the shear relative to stratification limited) by holding Ri^U constant but making the boundary layer thicker. Further, the need to

TABLE 2. Upwelling Ekman transport model runs.

Run No.	$N^2 \times 10^4$ (s^{-2})	$f \times 10^4$ (s^{-1})	v_I (cm s^{-1})	a	s	d	Numerical h (m)	Numerical h^{U*} (m)
80	0.9515	1.00	−20.0	0.0050	0.49	0.28	8.5	6.0 C
87	0.9515	1.00	−20.0	0.0025	0.24	0.28	9.9	8.7 C
88	0.9515	1.00	−20.0	0.0100	0.98	0.28	5.9	7.4 S
89	0.9515	1.00	−20.0	0.0005	0.05	0.28	15.1	13.3 C
89a	1.9029	1.00	−20.0	0.0050	0.69	0.40	6.7	4.2 C
180	2.8544	1.00	−10.0	0.0050	0.84	0.49	3.3	2.0 C
181	2.8544	1.00	−15.0	0.0100	1.69	0.49	4.3	4.2 S
182	1.9029	1.00	−30.0	0.0100	1.38	0.40	8.9	9.4 S
183	0.9515	0.30	−40.0	0.0005	0.16	0.95	31.5	36.6 C
184	0.9515	1.00	−30.0	0.0005	0.05	0.28	23.3	19.9 C
185	0.9515	0.30	−20.0	0.0005	0.16	0.95	16.1	18.3 C
186	0.9515	0.36	−40.0	0.0006	0.16	0.80	29.7	33.7 C
187	0.9515	0.30	−20.0	0.0010	0.33	0.95	13.7	13.1 C
188	0.9515	0.30	−20.0	0.0030	0.98	0.95	11.1	7.9 C
189	0.9515	1.00	−30.0	0.0060	0.59	0.28	11.7	8.0 C
197	0.9515	1.00	−30.0	0.0055	0.54	0.28	11.9	8.5 C
198	0.9515	1.00	−30.0	0.0065	0.63	0.28	11.5	8.3 C
199	0.9515	0.40	−30.0	0.0033	0.80	0.70	15.1	9.8 C
220	0.9515	1.43	−30.0	0.0116	0.79	0.20	10.3	9.7 S
221	0.4900	1.40	−30.0	0.0200	0.70	0.10	14.5	17.8 S
222**	0.9515	1.40	−30.0	0.0116	0.81	0.15	9.5	9.9 S
223	0.4757	1.00	−20.0	0.0029	0.20	0.20	12.7	10.1 C
224	1.6746	0.50	−40.0	0.0054	1.39	0.75	14.1	11.4 S
225	1.4547	0.50	−30.0	0.0066	1.59	0.70	14.5	13.0 S
226	1.0466	0.30	−30.0	0.0010	0.34	0.99	18.9	20.8 C

* The larger of h^{UC} or h^{US} is used. If the boundary layer is capped, the letter C appears. If it is smooth, the letter S appears.
** This model run uses $c_D = 2.2 \times 10^{-3}$; all others use 2.9×10^{-3}.

adjust to a thicker layer accounts for the tendency for smooth upwelling boundary layers to undergo a thickness jump at some relatively early time (Fig. 6a).

Our present results can be readily compared with Eq. (28a), which derives from MR96. As an example, we fix f, ρ_{Iz}, and v_I and vary the bottom slope α so as to isolate the dependence on the Burger number s. The results (Fig. 9b) show that the simple MR96 result replicates h^{UC} to within about a meter for this example. The expression for h^{MR} [in (28a)] fails for $s > 0.9$ when our formulation (47) switches over to h^{US} as the boundary layer thickness. Thus, (28a) is a useful approximation only for $h^{MR} > h^{US}$. Because the results for boundary layer thickness are comparable between our h^{US} and h^{MR}, the buoyancy adjustment time scales (45) and (29) are also quite comparable, even though this is not obvious given the rather different algebraic forms.

The overall collapse of scaled bottom stress versus nondimensionalized time (with the natural oscillations averaged out) using (34), (37), (44), and (45) is displayed as the negative values in Fig. 5. The capped and smooth cases have distinct φ functions, so that the upwelling case collapses to two curves rather than just one. Further, there is scatter at smaller times in the capped case because of the breakdown of the assumption that π/f^* is small relative to the buoyancy adjustment time. The scatter about the mean φ curves is 0.007 and 0.025 for the smooth and capped cases, respectively.

6. Summary

The primary results of the present analysis are improved formulations for the turbulent bottom boundary layer thickness in response to steady along-isobath flow. In the case of downslope Ekman transport ($v_I > 0$; Fig. 10a), the new Eq. (22) is a straightforward modification of the TL91 version, and it follows directly from the Lentz and Trowbridge (1991) comment that observations show that the downwelling bottom boundary layer tends to remain stably stratified. Our improved formulation differs increasingly from TL91 as the Burger number s (scaled bottom slope) increases (Fig. 9a).

The case with upslope Ekman transport ($v_I < 0$) is more involved (Fig. 9b). We find that, for a relatively large s, the final arrested boundary layer density profile is essentially linear (Fig. 10b) and that it joins smoothly to the interior density profile. In this case, the boundary layer has a fixed time-averaged gradient Richardson

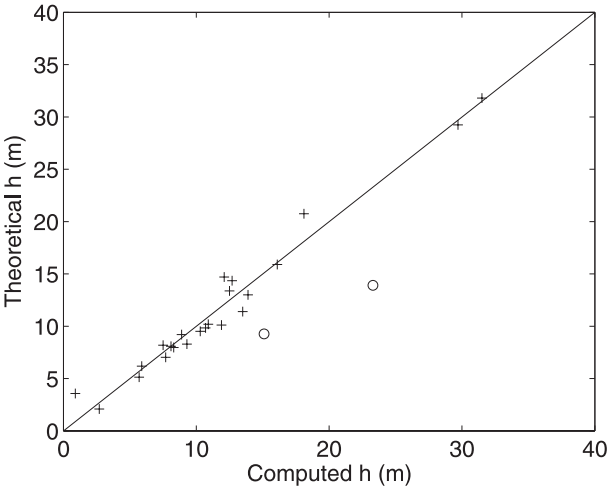

FIG. 7. Comparison of numerical model results for boundary layer thickness (defined for each run as the larger of either the height of maximum density gradient or of the height where turbulence vanishes) vs the present theory [expressed in Eqs. (34) and (44); crosses]. The circles indicate cases where $s < 0.1$. The present theory compares with model results to an rms misfit of 1.6 m for 23 model runs having $s > 0.1$.

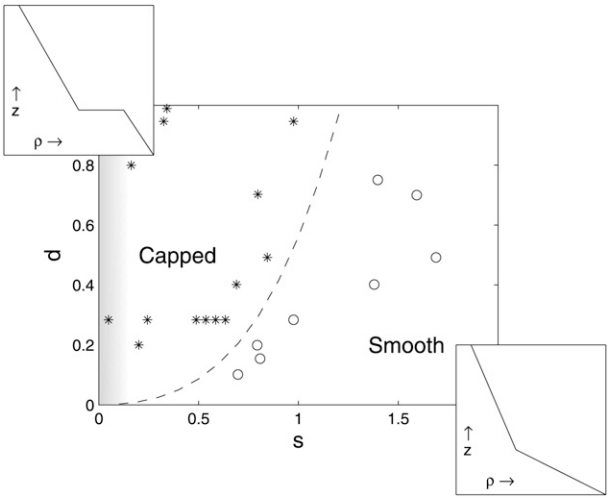

FIG. 8. Regime diagram for the boundary layer structure in the upwelling case. The dashed line separating the regimes is from inequality (48). The shaded area for small s indicates the parameter range where the capped boundary layer thickness exceeds h^{UC} and approaches that found at large times over a flat bottom.

number of 0.4, and a simple formula for the boundary layer thickness (34) is obtained. It is rather striking that this result, applying when Ekman transport leads to strong gravitational stability, so nearly parallels that found in the downwelling case where the mixing is primarily due to gravitational instability. In either case, the shear in the bottom boundary layer is distributed evenly across the layer, and the thickness is ultimately governed by a gradient Richardson number.

For smaller s, the final, buoyancy-arrested density state for an upwelling boundary layer has a sharp cap at the top of the layer (Fig. 10c), adjoining a continuously stratified boundary layer interior. In his case, the dominant shear in the bottom boundary layer is associated with the cross-isobath boundary layer transport, and it occurs sharply across the top of the layer. The physical content of the formulation leading to (44) elucidates how the bottom mixed layer is largely stabilized by cross-isobath buoyancy transport. In fact, before the onset of mixed layer stratification, the density contrast at the top of the layer increases with time, whereas the Ekman transport starts to decline because of arrest. It thus follows that there is some critical time, relatively early in the adjustment process, when the bulk Richardson number reaches its minimum value and the boundary layer reaches its maximum thickness.

One striking aspect of the present results is that the downwelling and smooth upwelling cases give rise to different gradient Richardson numbers. At first glance, this result is troublesome, because one might expect a critical gradient Richardson number of about 0.25 to apply universally. The resolution, however, is that the gradient Richardson numbers used in (22) and (34) are not instantaneous values but rather apply to the density and velocity fields averaged over a natural oscillation period $2\pi/f^*$. Over the course of an oscillation, in these cases, the Richardson number typically ranges from near zero to much larger numbers; therefore, the eddy viscosity periodically ranges from very substantial to near background values.

Because the present model formulation is one dimensional, the question naturally arises as to whether a more realistic two- or three-dimensional system would allow similar results. Allen and Newberger (1996) found that, in a two-dimensional numerical model with downwelling bottom Ekman transport, the flow is unstable to slantwise convection through symmetric instability. In contrast, upwelling bottom boundary layer flow is evidently stable in their runs (Allen et al. 1995). Allen and Newberger (1998) show that a necessary condition for instability is that the potential vorticity

$$\Pi = (f + v_x)\rho_z - v_z\rho_x > 0 \tag{49}$$

somewhere in the domain. If, in the downwelling case, the bottom boundary layer is unstratified, this condition holds true and the flow is unstable. Using the more realistic assumption of a constant density gradient, the adjusted state has $\rho_z = \rho_{Iz}\mathrm{Ri}^D s^2/\Gamma^2$ and

$$\Pi = -fs^2\rho_{Iz}[1 - \mathrm{Ri}^D(1 + s^2)/\Gamma^2]. \tag{50}$$

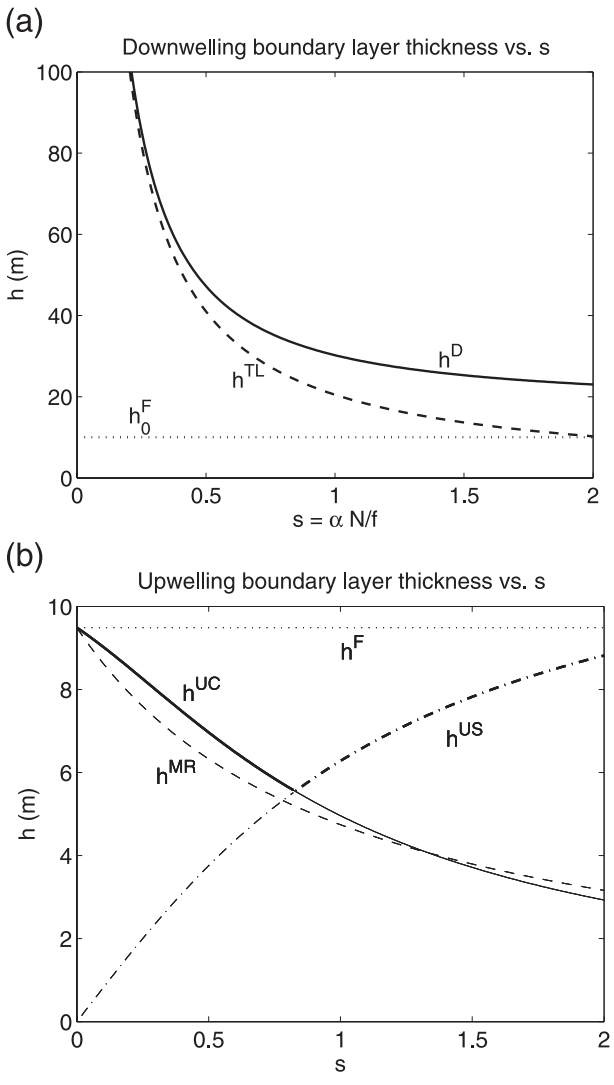

FIG. 9. (a) Theoretical downwelling boundary layer thickness as a function of s for $d = 0.28$. Parameters used are $f = 1 \times 10^{-4}$ s^{-1}, $\rho_{Iz} = -1 \times 10^{-7}$ gm cm^{-3}, and $v_I = 20$ cm s^{-1}. The bold curve h^D represents the current theory (22), the dashed curve h^{TL} is the TL91 result (12), and the dotted curve h_0^F is the flat-bottom result (28b). (b) Theoretical upwelling boundary layer thickness as a function of s for $d = 0.28$. Parameters used are $f = 1 \times 10^{-4}$ s^{-1}, $\rho_{Iz} = -1 \times 10^{-7}$ gm cm^{-3}, and $v_I = -20$ cm s^{-1}. The solid line is the capped thickness (h^{UC}: 44a), the dashed line is the MR96 thickness [h^{MR}; (28a)], the dashed–dotted line is the smooth boundary layer thickness [h^{US}; (34)], and the dotted line is the flat-bottom boundary layer thickness [h_0^F; (28b)]. The heavy lines represent the theoretical values for boundary layer thickness, given the selection criterion of picking the larger of h^{UC} or h^{US}. Note the difference in vertical scale between (a) and (b).

The resulting Π for the adjusted layer with $\mathrm{Ri}^D = 0.7$ remains in the unstable range for $s < 30$; however, Π is now closer to the stability boundary. In the smooth upwelling case, it is also straightforward to compute the boundary layer potential vorticity for the adjusted state, and the flow is symmetrically stable for all s. Further, regardless of whether the transport is upwelling or downwelling, there is always at least a part of the bottom boundary layer that is vertically homogeneous before a final state is reached, so it appears that some transient instability is always possible, if only briefly, as part of the adjustment process. However, the downwelling case's clear instability suggests that, in nature, the exact one-dimensional conditions leading to (22) should not be expected.

On a larger, shelf-wide scale, it is not certain how useful the present one-dimensional models will prove. For example, a two-dimensional (onshore and vertical) steady state requires that the surface and bottom stresses be equal. Thus, in the Allen et al. (1995) study, upslope Ekman transport eventually erases cross-isobath density gradients at the bottom, so that arrest cannot occur and bottom stress remains finite. The three-dimensional results of Middleton and Leth (2004) also appear to be evolving in this same direction. At shelf breaks, extreme cross-shelf gradients can occur, and the findings of Romanou and Weatherly (2001) give useful guidance on how boundary layer flow separates under these circumstances.

The results over a sloping bottom represent a sharp contrast with expectations for boundary layers over a flat bottom. When there is no bottom slope, the boundary layer is simply a well-mixed layer with a sharply defined density cap. In all cases over a sloping bottom, the boundary layer starts out well mixed shortly after the interior flow is initialized, but the boundary layer eventually becomes stably stratified, starting at the top of the layer and working downward (Fig. 10). The time scale for this adjustment, of course, varies strongly with s (hence bottom slope) and friction d, and it is effectively this adjustment time scale, compared to the time scale of interest to the observer, that determines whether the bottom is effectively flat. If s is small enough, in either the upwelling or downwelling cases, the adjustment time scales are long (on the order of a year) and the boundary layer is capped and well-mixed for extended times. In this sense, cases with small s approach flat-bottom conditions at times shorter than the adjustment time. Regardless of whether the flow is upwelling or downwelling favorable, the final, buoyancy-arrested state at long times is stably stratified. Only in the upwelling-favorable case with smaller s does a lasting density cap form at the top of the bottom boundary layer. The time- and depth-scale asymmetries between the upwelling and downwelling cases raise questions about what might be expected to happen with oscillating forcing, and these are dealt with in detail by Part II.

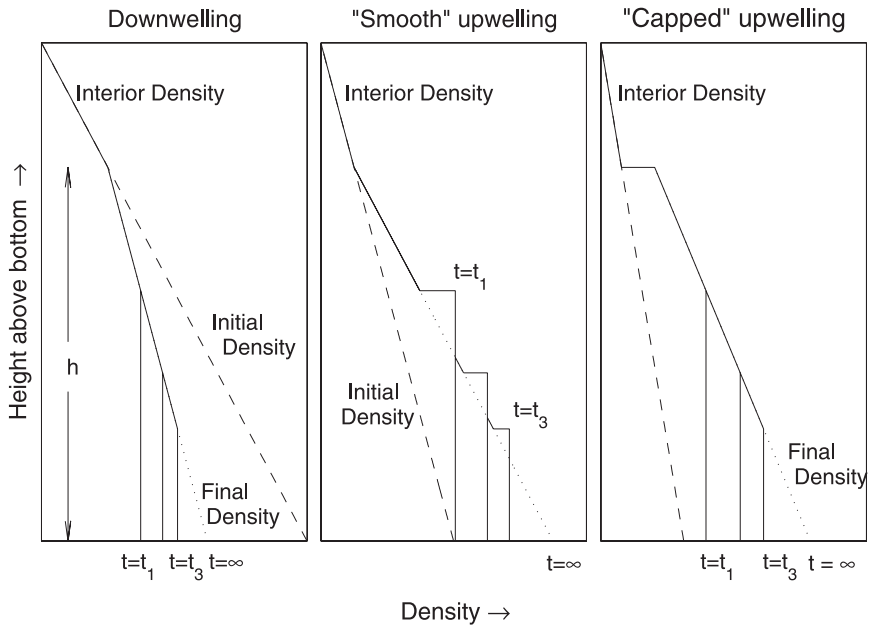

FIG. 10. Schematics showing the evolution of the density field during (left) downwelling, $v_I > 0$; (middle) smooth upwelling; and (right) capped upwelling, $v_I < 0$.

Acknowledgments. This research was supported by the National Science Foundation Physical Oceanography program through Grant OCE 0647050. We thank John Middleton and an anonymous reviewer for helpful comments.

APPENDIX

Review of Results for a Flat Bottom

Over a flat bottom, the physics of boundary layer deepening is analogous to conditions in a surface mixed layer with no surface heat flux. Thompson (1973) thus treats a slab-like bottom mixed layer and shows that the maximum shear across the top of the layer occurs at $t = \pi/f$. He closes the problem by assuming a critical bulk Richardson number, and (28b) results. His boundary layer thickness reaches its maximum at $t = \pi/f$, and turbulence is only generated in conjunction with shear across the top of the mixed layer.

The flat-bottom numerical initial-value problem yields a more complicated result (Fig. A1, solid lines). The layer thickens rapidly for the first half inertial period but then continues to thicken gradually. With Mellor–Yamada 2.0 turbulence closure (which does not diffuse turbulent kinetic energy), a steady boundary layer thickness of about 15 m is reached by about day 6. With Mellor–Yamada 2.5 closure (which diffuses turbulent kinetic energy), the boundary layer continues thickening, and it does not reach a steady thickness even by day 25. Using k–ε closure yields almost indistinguishable results compared to level 2.5 closure.

Physically, turbulence can be generated three ways in this problem: shear at the top of the layer (through

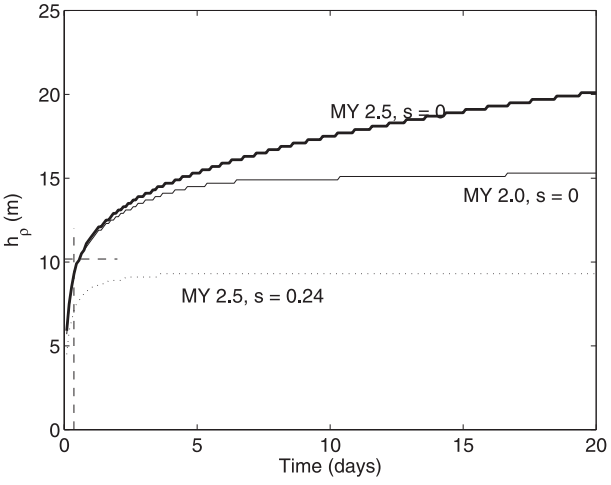

FIG. A1. Time series of bottom boundary layer thickness (defined as the height of maximum density gradient) vs time for three model runs with $f = 1 \times 10^{-4}$, $\rho_{Iz} = -1 \times 10^{-7}$, and $v_I = -20$ cm s^{-1}. The solid lines both have a flat bottom ($\alpha = 0$) but use either Mellor–Yamada 2.5 turbulence closure (heavy line) or 2.0 closure (lighter line). The dotted line has $\alpha = 0.0025$ ($s = 0.24$) and uses level 2.5 turbulence closure. The short horizontal dashed line is the flat-bottom boundary layer thickness (28b) for $R_b = 2$, and the vertical dashed line is at half an inertial period π/f. Only the first 20 days of the runs are shown.

Kelvin–Helmholtz instability), shear within the boundary layer (governed by a gradient Richardson number criterion), and shear at the bottom boundary itself. Because of the difference between Mellor–Yamada 2.0 and 2.5 closures, we conclude that continued growth in boundary layer thickness is due to bottom-generated turbulence diffusing to the top of the boundary layer, analogous to the Kraus–Turner deepening stage in a surface mixed layer problem (see Niiler 1975). Over a sloping bottom, buoyancy arrest ought to bring the bottom velocity to rest and therefore preclude this continued erosion. This conclusion is verified (Fig. A1) by comparing the Mellor–Yamada 2.5 runs with a flat bottom (heavy solid line, $s = 0$) to a case where arrest occurs (dotted line, $s = 0.24$). The exception to this turbulence shutdown is in our upwelling runs with $s < 0.1$, where shutdown occurs so slowly that the bottom-generated turbulence continues to be important until relatively large times.

REFERENCES

Allen, J. S., and P. Newberger, 1996: Downwelling circulation on the Oregon continental shelf. Part I: Response to idealized forcing. *J. Phys. Oceanogr.,* **26,** 2011–2035.

——, and ——, 1998: On symmetric instabilities in oceanic bottom boundary layers. *J. Phys. Oceanogr.,* **28,** 1131–1151.

——, ——, and J. Federiuk, 1995: Upwelling circulation on the Oregon continental shelf. Part I: Response to idealized forcing. *J. Phys. Oceanogr.,* **25,** 1843–1866.

Brink, K. H., and S. J. Lentz, 2010: Buoyancy arrest and bottom Ekman transport. Part II: Oscillating flow. *J. Phys. Oceanogr.,* **40,** 636–655.

Garrett, C., P. MacCready, and P. B. Rhines, 1993: Boundary mixing and arrested Ekman layers: Rotating stratified flow near a sloping bottom. *Annu. Rev. Fluid Mech.,* **25,** 291–324.

Lentz, S. J., and J. H. Trowbridge, 1991: The bottom boundary layer over the northern California shelf. *J. Phys. Oceanogr.,* **21,** 1186–1201.

MacCready, P., and P. B. Rhines, 1991: Buoyant inhibition of Ekman transport on a slope and its effect on stratified spin-up. *J. Fluid Mech.,* **223,** 631–661.

——, and ——, 1993: Slippery bottom boundary layers on a slope. *J. Phys. Oceanogr.,* **23,** 5–22.

Middleton, J. F., and D. Ramsden, 1996: The evolution of the bottom boundary layer on the sloping continental shelf: A numerical study. *J. Geophys. Res.,* **101** (C8), 18 061–18 077.

——, and O. K. Leth, 2004: Wind-forced setup of upwelling, geographical origins, and numerical models: The role of bottom drag. *J. Geophys. Res.,* **109,** C12019, doi:10.1029/2003JC002126.

Niiler, P. P., 1975: Deepening of the wind-mixed layer. *J. Mar. Res.,* **33,** 405–422.

Pacanowski, R. C., and G. H. Philander, 1981: Parameterization of vertical mixing in numerical models of the tropical oceans. *J. Phys. Oceanogr.,* **11,** 1443–1451.

Ramsden, D., 1995: Response of an oceanic bottom boundary layer on a slope to the interior flow. Part I: Time-independent interior flow. *J. Phys. Oceanogr.,* **25,** 1672–1687.

Romanou, A., and G. L. Weatherly, 2001: Numerical simulations of buoyant Ekman layers in the presence of variable stratification. Part I: Constant interior forcing. *J. Phys. Oceanogr.,* **31,** 3096–3120.

Tandon, A., and C. Garrett, 1994: Mixed layer restratification due to a horizontal density gradient. *J. Phys. Oceanogr.,* **24,** 1419–1424.

Thompson, R. O. R. Y., 1973: Stratified Ekman boundary layer models. *Geophys. Fluid Dyn.,* **5,** 201–210.

Thorpe, S. A., 1987: Current and temperature variability on the continental slope. *Philos. Trans. Roy. Soc. London,* **323A,** 471–517.

Trowbridge, J. H., and S. J. Lentz, 1991: Asymmetric behavior of an oceanic boundary layer above a sloping bottom. *J. Phys. Oceanogr.,* **21,** 1171–1185.

Weatherly, G. L., and P. J. Martin, 1978: On the structure and dynamics of the oceanic bottom boundary layer. *J. Phys. Oceanogr.,* **8,** 557–570.

Wijesekera, H. W., J. S. Allen, and P. A. Newberger, 2003: A modeling study of turbulent mixing over the continental shelf: Comparison of turbulent closure schemes. *J. Geophys. Res.,* **108,** 3103, doi:10.1029/2001JC001234.

Wimbush, M., and W. Munk, 1970: The benthic boundary layer. *The Sea,* M. N. Hill, Ed., New Concepts of Sea Floor Evolution, Part I: General Observations, Vol. 4, John Wiley and Sons, 731–758.